INTERNATIONAL JOURNAL FOR NUMERICAL METHODS IN FLUIDS
Int. J. Numer. Meth. Fluids 2007; **54**:995–1009
Published online 19 April 2007 in Wiley InterScience (www.interscience.wiley.com). DOI: 10.1002/fld.1497

Numerical investigation of the effect of hypertensive blood pressure on cerebral aneurysm—Dependence of the effect on the aneurysm shape

Ryo Torii[1,*,†], Marie Oshima[2], Toshio Kobayashi[3], Kiyoshi Takagi[4] and Tayfun E. Tezduyar[5]

[1]*Department of Chemical Engineering, Imperial College, South Kensington Campus, London SW7 2AZ, U.K.*
[2]*Institute of Industrial Science, The University of Tokyo, 4-6-1 Komaba, Meguro, Tokyo 153-8505, Japan*
[3]*Japan Automobile Research Institute, 2530 Karima, Tsukuba, Ibaraki 305-0822, Japan*
[4]*Department of Neurosurgery, Ogura Hospital, 4-2-5 Nakamachi, Setagaya, Tokyo 158-8585, Japan*
[5]*Mechanical Engineering, Rice University—MS 321, 6100 Main Street, Houston, TX 77005, U.S.A.*

SUMMARY

Fluid–structure interaction (FSI) computations of two cerebral aneurysms are carried out under hypertensive and normotensive blood pressures. Hypertensive blood pressure is one of the major risk factors in subarachnoid hemorrhage, which is mostly caused by the rupture of cerebral aneurysm. Since hemodynamic wall shear stress (WSS) is known to play an important role in aneurysm progression, investigating the WSS distribution in conjunction with hypertensive blood pressure is expected to provide a better understanding of aneurysms. The WSS distributions obtained from the simulations show that hypertensive blood pressure considerably affects one of the subjects but not the other. The effect is a wider spreading of the high WSS region on the aneurysm wall, which prevents the wall from weakening. It is also shown that the deformation of the aneurysm wall can alter the flow patterns in the aneurysm to diminish the stagnant flow near the apex, which is linked to the weakening of the wall. The effect of hypertensive blood pressure and wall deformation is shown to be highly dependent on individual aneurysm geometry, and that stresses the importance of subject-specific simulations. Copyright © 2007 John Wiley & Sons, Ltd.

Received 23 January 2007; Revised 5 March 2007; Accepted 6 March 2007

KEY WORDS: cardiovascular modelling; fluid–structure interaction; patient-specific computation; hypertension; aneurysm shape

*Correspondence to: Ryo Torii, Department of Chemical Engineering, Imperial College, South Kensington Campus, London SW7 2AZ, U.K.
†E-mail: r.torii@imperial.ac.uk

Contract/grant sponsor: Ministry of Education, Culture, Sports, Science and Technology (MEXT)

1. INTRODUCTION

Cerebral aneurysm—its rupture is the leading cause of subarachnoid hemorrhage (SAH) [1] and is known to be induced by blood flow [2]. In particular, the wall shear stress (WSS) serves as a link between the blood flow and the aneurysm because the arterial wall remodelling is controlled by the WSS acting on the endothelium [3]. The importance of the blood flow in aneurysm progression was also shown by statistical data. The aneurysm geometry characterized by the height, diameter, and neck width (or aspect ratio, AR = height/neck width) is reported to indicate the progression and rupture risk of aneurysms [4, 5]. Ujiie *et al.* [4] particularly connected the aneurysm progression to blood-flow stagnation owing to the aneurysm geometry. Although hemodynamics in cerebral aneurysms has been investigated experimentally [4, 6] and computationally [7–11], to better understand the aneurysm progression, the mechanism still needs more comprehensive investigation. Researchers now expect numerical simulation to be an effective tool in investigating hemodynamics in more detail. That is because measuring hemodynamics in and resulting WSS on tiny cerebral aneurysms *in vivo* is still difficult. Also, more sophisticated computational techniques, and more powerful computational resources are becoming available.

Computational work focusing on hemodynamics in aneurysms can be carried out at different levels of approximation. Studies using idealized models [7, 8, 12] with idealized geometries and flow conditions require less computational resources and can support parametric studies. Studies using realistic geometries and flow conditions [9, 10, 13], including the fluid–structure interaction (FSI) modelling [11, 14–16] in arterial fluid mechanics, occasionally coupled with mass transfer [17], are closer to reality but require more computational resources. The FSI modelling is crucial in accurate computation of the dynamics of the blood flow, the arterial wall deformation and the interaction between the two. Fortunately much has been accomplished in recent decades in the development of advanced computational techniques for FSI modelling and their parallel implementation for efficient, high-speed computations (see, for example, [15, 18–35]). In an attempt to have the advantages of both the idealized and realistic simulations, we have been working on FSI simulations with realistic aneurysm models coupled with parameter changes representing the changes in physiological conditions. We have been particularly focusing on the interaction between the blood flow and the arterial wall deformation under high and normal blood pressure conditions [11], because hypertension is one of the major risk factors in SAH [1, 36]. In this paper, we apply hypertensive and normotensive blood pressure conditions to two patient-specific aneurysm models to investigate how differently high blood pressure works on those aneurysms.

2. COMPUTATIONAL METHOD

The blood flow in cerebral arteries is assumed to be laminar [37] and governed by the Navier–Stokes equations of incompressible flows. The fluid mechanics with moving and deforming walls is computed with the deforming-spatial-domain/stabilized space–time (DSD/SST) method [18–20, 25]. In the DSD/SST formulation, the streamline-upwind/Petrov–Galerkin (SUPG) [38, 39] and pressure-stabilizing/Petrov–Galerkin (PSPG) [18, 40] formulations are employed for stabilization. The DSD/SST method was introduced for flows with moving boundaries and interfaces and has been applied to a large class of problems [41–48], including FSI [21–24, 28, 35, 49].

The structural mechanics is governed by the force equilibrium equations and computed with the Galerkin finite element method. The arterial structure is modelled as geometrically non-linear, made of linearly elastic material.

DOI: 10.1002/fld

The fluid and structural mechanics systems are coupled at the interface by kinematic and dynamic conditions. The two systems are solved with a block-iterative coupling approach [28, 50]. The fluid mesh is updated by using an automatic mesh moving method [41, 51], where the motion of the nodal points is governed by the equations of elasticity. The boundary conditions come from the motion of the interface between the fluid and structure. Details of the computational method are described in [14].

3. COMPUTATIONAL MODEL

We reconstructed two aneurysm models at the middle cerebral artery (MCA) bifurcation based on CT images (provided by Dr Motoharu Hayakawa, Fujita Health University). The models are shown in Figure 1. Subject 1 is a 59-year-old female; the aneurysm was ruptured before it was scanned. Subject 2 is a 67-year-old female; the aneurysm is unruptured.

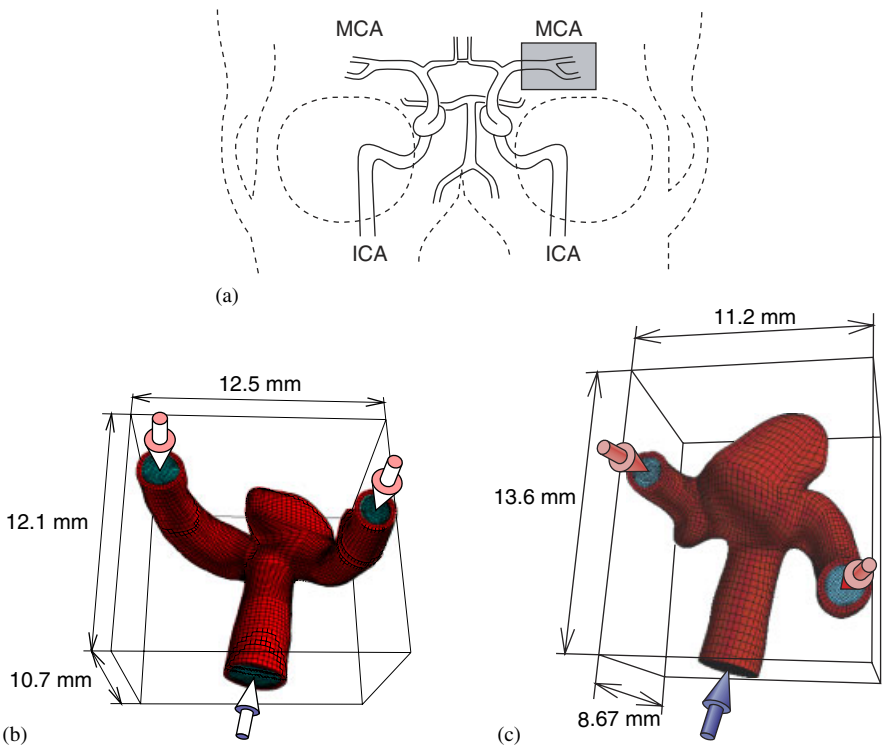

Figure 1. Aneurysm models based on CT images: (a) cerebral arterial network and the location of the middle cerebral artery (MCA). The internal carotid artery (ICA) provides the main blood supply to the cerebral arterial network, branching off of the common carotid artery; (b) and (c) aneurysm models for Subject 1 (59-year-old, female, ruptured aneurysm) and Subject 2 (67-year-old, female, unruptured aneurysm). The blue arrow denotes the inflow direction and the red arrows the resistance at the outlet from the distal arterial network.

DOI: 10.1002/fld

Table I. Geometric features of the aneurysms.

Subject	$d_{\max}$ (mm)	d_n (mm)	h (mm)	AR
1	5.64	3.99	2.93	0.73
2	4.90	2.57	7.22	2.81

Note: Here $d_{\max}$, d_n and h are the maximum diameter, neck width and height. Aspect ratio, $\mathrm{AR} = h/d_n$.

Table II. Number of nodes and elements used in the computations.

Subject	$N_{\mathrm{n}}^{\mathrm{f}}$	$N_{\mathrm{e}}^{\mathrm{f}}$	$N_{\mathrm{n}}^{\mathrm{s}}$	$N_{\mathrm{e}}^{\mathrm{s}}$
1	49 395	46 000	11 520	10 800
2	53 769	50 240	17 397	11 480

Note: Here N_{n} and N_{e} are the number of nodes and elements, and the subscripts f and s denote the fluid and structure.

Approximately 150 CT slices with 0.60 mm intervals were used for the geometry reconstruction. Each slice consists of 512×512 pixels. The in-plane resolution of a slice is 0.3125 mm/pixel. The surface of the arterial lumen was then constructed with the matching-cubes method [52] as an iso-surface at a certain CT signal intensity representing the arterial lumen. The reconstruction process was carried out with the commercial software ALATOVIEW (Toshiba Medical, Inc.). Because the arterial wall is invisible with the CT, it was added by assuming a uniform wall thickness of 0.3 mm and inflating the luminal wall outward. The arterial wall and the lumen for the two subjects are shown in red and blue in Figure 1. The diameter of the arterial lumen at the inlet is 2.74 for Subject 1 and 2.38 mm for Subject 2. At the distal end, the diameter ranges from 1.51 to 2.01 mm. The diameter, height, neck width ($=$ diameter at the open mouth of the aneurysm) and the resulting aspect ratio are summarized in Table I. Comparing the aspect ratios with what was reported in Ujiie *et al.* [4], Subject 1 shows the typical geometric features of an unruptured aneurysm. On the other hand, the aspect ratio for the Subject 2 is within the typical range of a ruptured aneurysm.

Eight-node hexahedral elements are used for the finite element discretization as shown in Figure 1. We employ first-order interpolation functions for all variables. The number of nodes and elements are summarized in Table II.

4. MECHANICAL PROPERTIES AND BOUNDARY CONDITIONS

Although the blood is known to be non-Newtonian in general, we assume it to be Newtonian in this study. We are focusing on arteries with diameters and flow rates nearly equal to 3.0 mm and 2.0 ml/s, respectively. Hence the averaged shear rate in the arteries is approximately $\dot{\gamma} = 4Q/(\pi R^3) \sim 755\ \mathrm{s}^{-1}$ (Q and R are flow rate and radius). The viscosity of the blood can be approximated as a constant when the shear rate in the flow is high enough ($>150\ \mathrm{s}^{-1}$) [53]. The density and kinematic viscosity of the blood are set to $1000\ \mathrm{kg/m^3}$ and $4.0 \times 10^{-6}\ \mathrm{m^2/s}$, respectively. The arterial wall is assumed to be made of linearly elastic material. The elastic modulus and Poisson ratio for the arterial wall are set to 1.0 MPa and 0.49.

DOI: 10.1002/fld

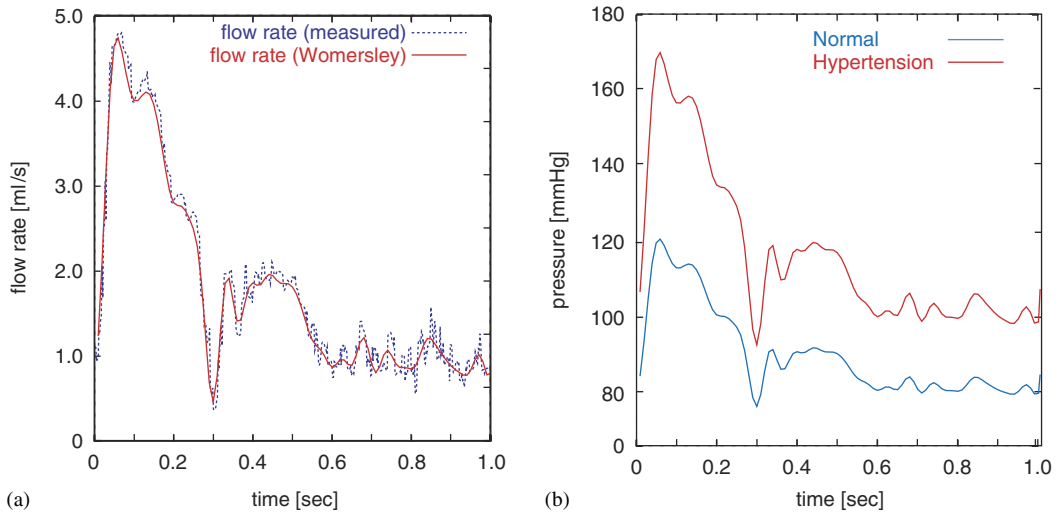

Figure 2. Flow (a) and pressure (b) waveforms. The flow waveform is based on the velocity measured at the common carotid artery with ultrasound Doppler velocimeter. The pressure waveform is determined based on the flow waveform to obtain the physiological range of pressure assuming that there is no phase lag.

The inflow boundary conditions are specified as a pulsatile velocity profile prescribed by Womersley's formulation [54]

$$w(r,t) = \frac{2B_0}{\pi R^2}\left[1-\left(\frac{r}{R}\right)^2\right] + \sum_{n=1}^{N}\frac{B_n}{\pi R^2}\left[\frac{1-J_0(\alpha_n(r/R)i^{3/2})/J_0(\alpha_n i^{3/2})}{1-2J_1(\alpha_n i^{3/2})/(\alpha_n i^{3/2}J_0(\alpha_n i^{3/2}))}\right]\mathrm{e}^{\mathrm{i}n\omega t} \tag{1}$$

$$Q(t) = \sum_{n=0}^{N} B_n \mathrm{e}^{\mathrm{i}n\omega t} \tag{2}$$

where r is the cylindrical coordinate at the inlet, t is time and R is the radius of the artery at the inlet. Here J_0 and J_1 are the Bessel functions of the first kind and of order 0 and 1, and $\alpha_n = R\sqrt{n\omega/\nu}$, where ω is the angular frequency of one cardiac cycle ($\omega = 2\pi$ rad/s). The parameter $\alpha = R\sqrt{\omega/\nu}$ is known as the Womersley parameter, which is the non-dimensional frequency of the pulsatile flow. The coefficients B_n are derived in reference to the velocity waveform with Fourier decomposition. The original velocity waveform was acquired with ultrasound Doppler at the carotid artery of a healthy volunteer in his 20s. Figure 2 shows the flow waveform based on the measured velocity, with the velocity profile modelled by the Womersley's formulation.

The pressure conditions applied at the outlet represent the resistance from the distal arterial network. These conditions are applied at the outlet as traction normal to the boundary, which are shown with red arrows in Figure 1. The pressure at the outlet varies with time, prescribed by a series of exponential functions, the same as those used in specifying the inflow conditions

$$P(t) = \sum_{n=0}^{N} P_n \mathrm{e}^{\mathrm{i}n\omega t} \tag{3}$$

DOI: 10.1002/fld

Here the coefficients P_n are determined, based on the coefficients B_n used for the inflow conditions, to produce the physiological range of 80–120 mmHg for a healthy male. The hypertensive blood pressure is modelled by changing the P_n to produce the range of hypertensive blood pressure, 110–170 mmHg. The pressure waveforms for the hypertensive (HBP) and normotensive (NBP) blood pressure conditions are shown in Figure 2. In this study, phase differences between the pressure and velocity fluctuations are not taken into account. At the interface between the blood and the arterial wall, no-slip conditions are applied in the fluid mechanics part and hemodynamic forces in the structural mechanics part. Only the pressure difference from the level at the beginning of the cardiac cycle is applied to the arterial wall. The boundary displacements at the inlet and two outlets of the artery are set to zero. Influence of the residual stress are not taken into account.

5. RESULTS AND DISCUSSION

5.1. Wall deformation

Figure 3 shows the displacement magnitude at the peak systole ($t = 0.06$ s). The maximum displacement at the peak systole is 0.752 mm (HBP) and 0.700 mm (NBP) for Subject 1 and 0.533 mm (HBP) and 0.361 mm (NBP) for Subject 2. For both subjects, the displacement is larger under HBP than it is under NBP. However, for Subject 1, the difference in the displacement due to

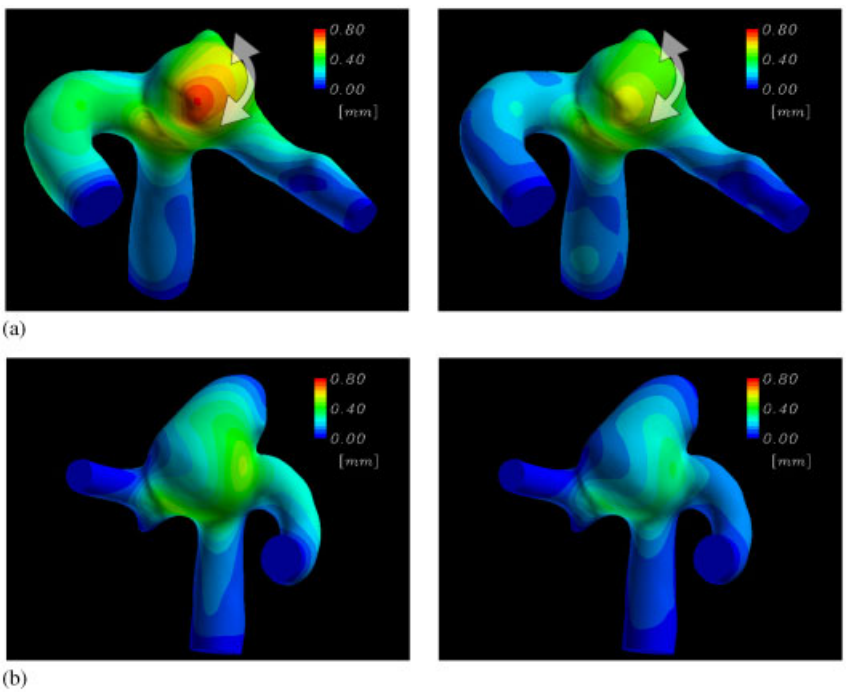

Figure 3. Displacement magnitude at the peak systole ($t = 0.06$ s) for: (a) Subject 1 and (b) Subject 2, with HBP (left) and NBP (right).

DOI: 10.1002/fld

the two pressure conditions during the systolic period is only 7.4%, although the systolic pressure rise for HBP (~ 60 mmHg) is 50% larger than that for NBP (~ 40 mmHg). That is because the displacement of the aneurysm of Subject 1 involves not only inflation but also a 'swinging motion,' as shown with the white arrows in the figure. Because the magnitude of the swinging motion is large compared to the magnitude of the inflation, and because the swinging motion is not significantly affected by the differences in pressure conditions, the difference in the maximum displacements under HBP and NBP was not as prominent as the difference in the pressure conditions. On the other hand, for Subject 2, the displacement of the aneurysm basically consists of inflation in its radial direction. The maximum displacement therefore is proportionally dependent on the pressure conditions. We can see that differences in the individual geometries of the aneurysms lead to significantly different trends in the aneurysm displacement. The two subjects are affected differently by hypertensive blood pressure.

5.2. WSS distribution

Figure 4 shows the WSS distributions at various instants near the peak systole. For Subject 1, at the peak systole, the WSS on the aneurysm is smaller under HBP than it is under NBP. However, immediately after the peak systole ($t = 0.07$ s), the WSS on the aneurysm is larger under HBP than it is under NBP. The maximum WSS does not occur at the peak systole but after that, and the high WSS region spreads more on the aneurysmal wall under HBP. There are two local maxima of WSS at $t = 0.07$ s; one on the aneurysm and the other on the wall of the left branch near the neck. Under HBP, the maximum WSS is 365 dyn/cm^2 on the branch and 398 dyn/cm^2 on the aneurysm. Under NBP, it is 324 dyn/cm^2 on the branch and 329 dyn/cm^2 on the aneurysm. Hypertensive blood pressure significantly alters the WSS distribution for Subject 1.

For Subject 2, the maximum WSS occurs at the peak systole on the wall of the left branch. The maximum WSS at the peak systole is 282 and 345 dyn/cm^2 under HBP and NBP. Unlike Subject 1, the WSS on the aneurysmal wall is always lower than the maximum WSS. There is a belt-like area of relatively high WSS at the middle of the aneurysm. The maximum WSS occurring at that area is 103 and 108 dyn/cm^2 for HBP and NBP. The WSS on the aneurysm is low apart from the belt-like area. In particular, the low WSS region at the top of the aneurysm is linked to the degrading of the wall and rupture of the aneurysm [4]. However, after the peak systole, the area of relatively high WSS starts spreading towards the top. The area spreads over the top half of aneurysm at $t = 0.10$ s, and the low WSS area at the top eventually disappears. The maximum WSS in that area is 146 and 144 dyn/cm^2 under HBP and NBP. The WSS for Subject 2 is lower under HBP than it is under NBP. Hypertensive blood pressure does not alter the WSS distribution for Subject 2, unlike what we see for Subject 1.

5.3. Flow velocity profile

Investigating the flow velocity profile helps in the understanding of the differences in the WSS due to the pressure conditions. Figure 5 shows the velocity profiles corresponding to the WSS distributions shown in Figure 4. For Subject 1, the blood flows from the inlet and impinges on the neck of the aneurysm at the bifurcation. Flow impingement at a bifurcation was pointed as key to understanding the relationship between hemodynamics and aneurysm because it produces a focal area of high WSS [8, 10]. We previously showed that the impinging flow is even more important in aneurysm hemodynamics when the wall deformation is taken into account [11, 16]. First, the deformation of the arterial wall proximal to the bifurcation affects the impinging flow

DOI: 10.1002/fld

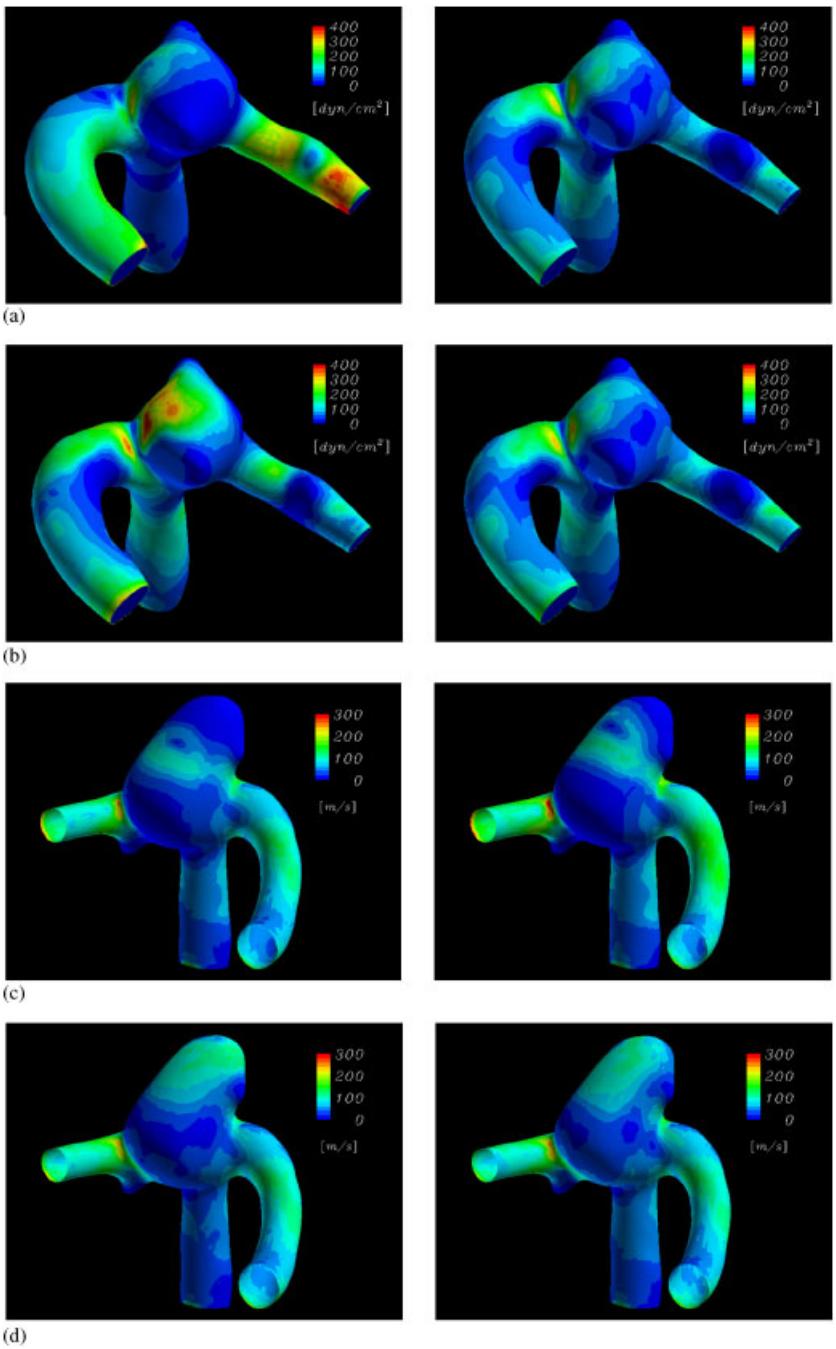

Figure 4. WSS distribution for Subject 1: (a) at the peak systole ($t = 0.06$ s) and (b) immediately after the peak systole ($t = 0.07$ s); and for Subject 2 (c) at the peak systole and (d) after the peak systole ($t = 0.10$ s), with HBP (left) and NBP (right).

DOI: 10.1002/fld

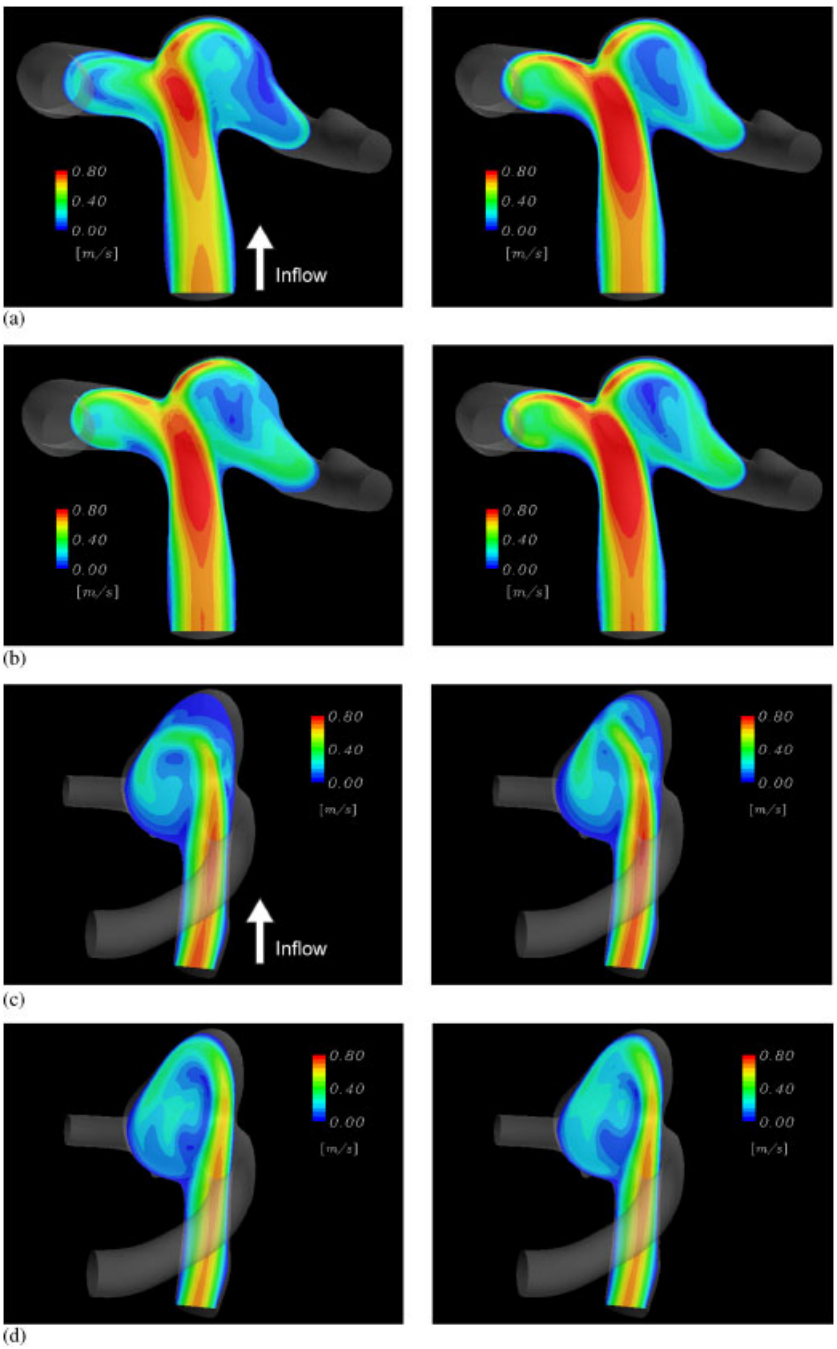

Figure 5. The velocity profiles for Subject 1: (a) at the peak systole ($t = 0.06$ s) and (b) immediately after the peak systole ($t = 0.07$ s); and for Subject 2 (c) at the peak systole and (d) after the peak systole ($t = 0.10$ s), with HBP (left) and NBP (right). Colours represent the velocity magnitude.

DOI: 10.1002/fld

velocity, i.e. the expansion of the artery slows the impinging flow down. Second, the deformation of the arterial wall near the impinging region can drastically alter the velocity gradient near the wall and the resulting WSS. Figure 5 shows that, under NBP, the blood flows at high velocity ($\sim 0.75\,\mathrm{m/s}$) into both the aneurysm and the left branch. When HBP is applied to Subject 1, the arterial wall near the impingement region deforms substantially at the peak systole. That enables more blood flow at high velocity into the aneurysm. Higher flow in the aneurysm results in higher velocity gradient near the wall and WSS on the aneurysmal wall. In addition, contraction of the arterial and aneurysm walls at $t = 0.07\,\mathrm{s}$ enlarges the velocity gradient near the wall. Since low WSS should degrade the aneurysm walls, the effect of hypertensive blood pressure is to prevent the arterial wall from degrading although there are low WSS regions remaining on the aneurysm.

For Subject 2, the blood flow does not impinge on the neck but enters straight into the aneurysm. Under both HBP and NBP, the flow impinges on the aneurysm wall and produces a belt-like high WSS region, forms a large vortex accompanied with a smaller secondary vortex at the top, and flows into the two branches. The velocity in the aneurysm becomes low as the blood flows further due to the sudden expansion of the cross-sectional area at the neck of the aneurysm. Particularly under HBP, the velocity in the top region of the aneurysm is extremely low because the expansion of aneurysm slows the main stream from the parent artery down and the flow cannot reach far into the aneurysm. However, after the peak systole, the direction of the flow into the aneurysm changes. The blood flow reaches the top region of the aneurysm along the wall. The secondary vortex, which is considered to be a typical flow pattern in an aneurysm with high aspect ratio, disappears. That is the reason why a belt-like high WSS region occurring in the middle of the aneurysm at the peak systole spreads on the top half of aneurysm. Because the flow profiles under HBP and NBP at $t = 0.10\,\mathrm{s}$ are similar, hypertensive blood pressure does not affect the trend of the flow velocity profile or the resulting WSS distribution.

5.4. Hemodynamic characteristics and arterial wall deformation

The aneurysm shape for Subject 2 shows typical features of an ruptured aneurysm (AR$>$1.6) [4], which causes recirculating flow with weak secondary recirculation in the top region of the aneurysm linked to the weakening of the aneurysm wall due to low WSS. However, our computational result shows that the secondary recirculation disappears after the peak systole. The WSS on the aneurysm wall is consequently large in the top region. We also computed the blood flow with rigid walls to investigate in more detail the hemodynamic features in the aneurysm of Subject 2. The reason why the secondary recirculation disappears would particularly be of interest.

Figure 6 shows the WSS distribution and flow velocity profile for the rigid-wall model at instants shown in Figures 4 and 5. At the peak systole, the flow at high velocity from the inlet impinges on the aneurysm wall, with a secondary recirculation in the top region. The flow profile stays similar even after the peak systole. The maximum WSS on the aneurysm at the peak systole is $162\,\mathrm{dyn/cm^2}$, which is higher than it is for the compliant-wall cases. This is the result of the flow impinging with higher velocity, not slowed down by the inflation of the artery and aneurysm. However, the WSS at the top of the aneurysm is lower for the rigid-wall cases due to the secondary recirculation.

Figure 7 compares, with magnification, the velocity profiles near the aneurysm for the rigid- and compliant-wall cases, and illustrates the relationship between the aneurysm geometry and

DOI: 10.1002/fld

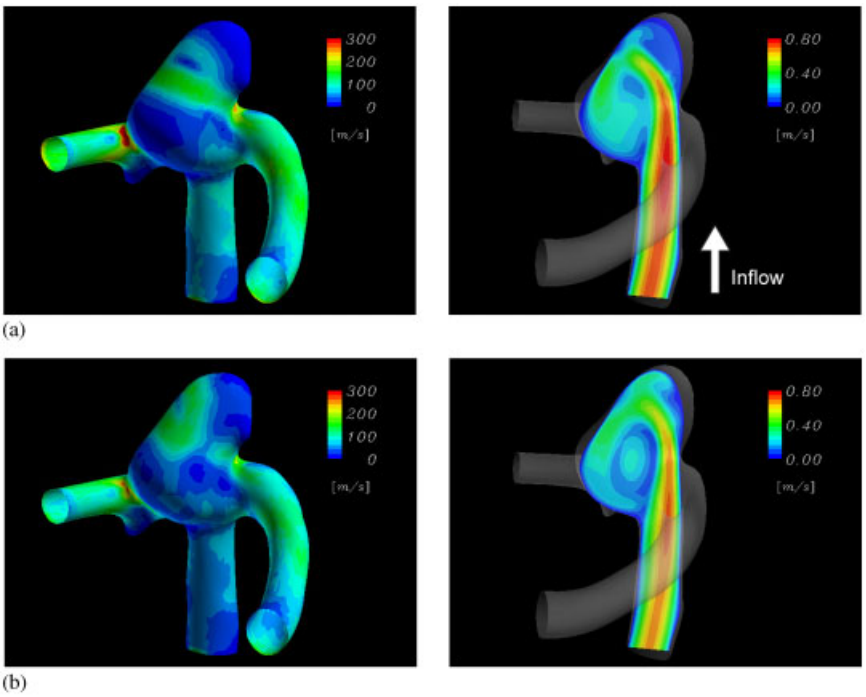

Figure 6. WSS distribution (a) and flow velocity profile (b) for Subject 2 with the rigid-wall model.

the flow patterns. The flow patterns at the peak systole are similar for all cases, i.e. the inflow is bent and impinges on the aneurysm. Because of the deformation of the aneurysm wall at the region indicated by the white arrow, under NBP the flow direction is slightly straighter towards the apex of the aneurysm. The flow direction under HBP is also towards the apex, but the flow velocity is too low to reach the top region because of the large inflation of the aneurysm. The wall deformation at the region pointed by the white arrow remains after the peak systole. That allows the flow to proceed straight along the wall and reach the apex of the aneurysm. For the rigid-wall case, on the other hand, the curvature of the aneurysm wall keeps the flow bent towards the wall on the other side. The secondary recirculation remains for the rigid-wall case. It is shown that the disappearance of the secondary recirculation is not because of the pulsatility in the flow but because of the wall compliance.

Although the aneurysm of Subject 2 has typical features of a ruptured aneurysm, it has been staying unruptured. The hemodynamic features obtained with the compliant-wall model shows the disappearance of the secondary recirculation linked to the degrading of the aneurysm wall. That could be the reason why the aneurysm did not rupture despite the geometric features typically seen in ruptured aneurysms. We previously reported in [11] that the effect of the wall deformation was not to alter the flow patterns in the aneurysm but to decrease the WSS at the focal area of high WSS. For Subject 2, the effect of wall deformation appears in a different way to alter the flow patterns in the aneurysm.

DOI: 10.1002/fld

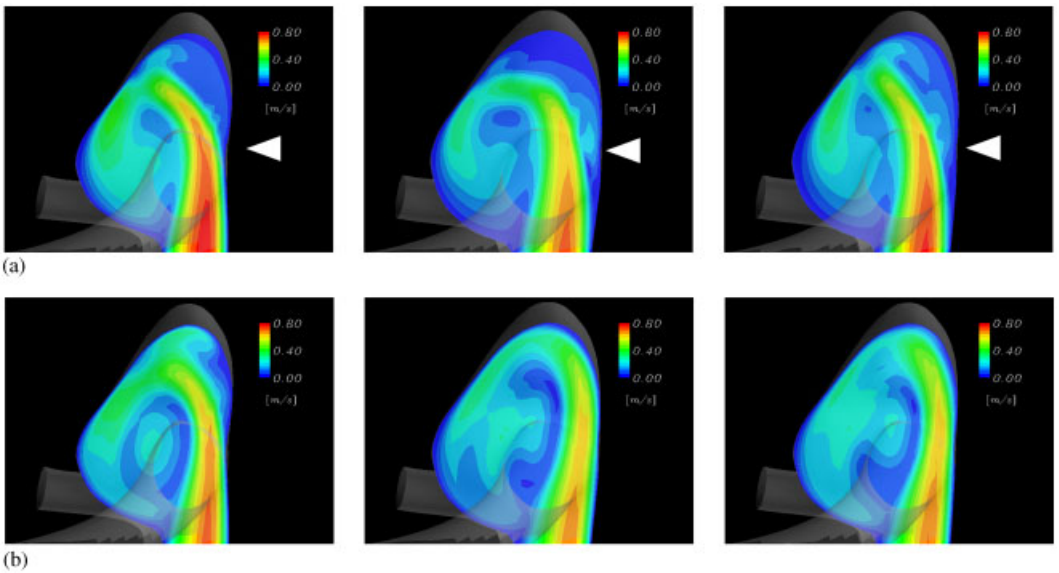

Figure 7. Comparison of the flow velocity profiles: (a) at the peak systole and (b) at $t = 0.10$ s, for the rigid-wall (left), HBP (middle) and NBP (right) cases.

6. CONCLUSIONS

Computational analyses of the interaction between the blood flow and the arterial/aneurysmal wall for two subjects under hypertensive and normotensive blood pressures were carried out. Our objective was to better understand the mechanism of disease progression with reference to hemodynamic WSS, particularly focused on the effects of hypertensive blood pressure, which is one of the risk factors in the rupture of aneurysms. The results show that hypertensive blood pressure has an influence for one of the subjects but not the other one. For the first subject, hypertensive blood pressure alters the WSS distribution on the aneurysm. The WSS is higher on the aneurysm under hypertensive blood pressure. For the second subject, on the other hand, the WSS on the aneurysmal wall is not altered by hypertensive blood pressure. The difference in the effects of hypertensive blood pressure is because of the relationship between the flow patterns and the nature of the wall deformation, e.g. the magnitude of the wall displacement at the location of the flow impingement. Although the influence of hypertensive blood pressure on the flow patterns is insignificant for the second subject, it is shown that the deformation of the aneurysm wall alters the flow patterns that are linked to the weakening of the aneurysm wall. This is consistent with the fact that the aneurysm of the second subject did not rupture despite its geometric features typically observed in ruptured aneurysms. The results show the importance of subject-specific simulations, because the interaction between the blood flow and the arterial wall deformation and the effect of hypertensive blood pressure very much depend on the individual aneurysm geometry.

ACKNOWLEDGEMENTS

Authors would be grateful to Dr Motoharu Hayakawa, Fujita Health University (Aichi, Japan) for providing CT and for his suggestions in terms of radiology. Authors also acknowledge Toshiba Medical, Inc., for

DOI: 10.1002/fld

providing image processing software ALATOVIEW. Part of this research was carried out within the framework of the project 'Frontier Simulation Software for Industrial Science (FSIS)', supported by the IT program of the Ministry of Education, Culture, Sports, Science and Technology (MEXT).

REFERENCES

1. van Gijn J, Rinkel GJE. Subarachnoid heamorrhage: diagnosis, cause and management. *Brain* 2001; **124**:249–278.
2. Steiger HJ. Pathophysiology of development and rupture of cerebral aneurysms. *Acta Neurochirurgica Suppliment* 1990; **48**:1–57.
3. Lehoux S, Tronc F, Tedgui A. Mechanisms of blood flow-induced vascular enlargement. *Biorheology* 2002; **39**:319–324.
4. Ujiie H, Tachibana H, Hiramatsu O, Hazel A, Matsumoto T, Ogasawara Y, Nakajima H, Hori T, Takakura K, Kajiya F. Effects of size and shape (aspect ratio) on the hemodynamics of saccular aneurysms: a possible index for surgical treatment of intracranial aneurysms. *Neurosurgery* 1999; **45**:119–130.
5. Russel SM, Lin K, Hahn SA, Jafar JJ. Smaller cerebral aneurysms producing more extensive subarachnoid hemorrhage following rupture: a radiological investigation and discussion of theoretical determinants. *Journal of Neurosurgery* 2003; **99**:248–253.
6. Tateshima S, Murayama Y, Villablanca JP, Morino T, Takahashi H, Yamauchi T, Tanishita K, Vinuela F. Intraaneurysmal flow dynamics study featuring an acrylic aneurysm model manufactured using a computerized tomography angiogram as a mold. *Journal of Neurosurgery* 2001; **95**:1020–1027.
7. Burleson AC, Strother CM, Turitto VT. Computer modeling of intracranial saccular and lateral aneurysms for the study of their hemodynamics. *Neurosurgery* 1995; **37**:774–783.
8. Foutrakis GN, Yonas H, Sclabassi RJ. Saccular aneurysm formation in curved and bifurcating arteries. *American Journal of Neuroradiology* 1999; **20**:1309–1317.
9. Shojima M, Oshima M, Takagi K, Torii R, Hayakawa M, Katada K, Morita M, Kirino T. Magnitude and role of wall shear stress on cerebral aneurysm: computational fluid dynamic study of 20 middle cerebral artery aneurysms *Stroke* 2004; **35**:2500–2505.
10. Cebral JR, Castro MA, Burgess JE, Pergolizzi RS, Sheridan MJ, Putman CM. Characterization of cerebral aneurysms for assessing risk of rupture by using patient-specific computational hemodynamics models. *American Journal of Neuroradiology* 2005; **26**:2550–2559.
11. Torii R, Oshima M, Kobayashi T, Takagi K, Tezduyar TE. Fluid–structure interaction modeling of aneurysmal conditions with high and normal blood pressures. *Computational Mechanics* 2006; **38**:482–490.
12. Zakaria H, Yonas H, Robertson AM. Analysis of the importance of the ratio of aneurysm size to parent artery diameter on hemodynamic condition. *Journal of Biomechanics* 2006; **39**:S272.
13. Taylor CA, Draney MT, Ku JP, Parker D, Steele BN, Wang K, Zarins CK. Predictive medicine: computational techniques in therapeutic decision-making. *Computer Aided Surgery* 1999; **4**:231–247.
14. Torii R, Oshima M, Kobayashi T, Takagi K, Tezduyar TE. Computer modeling of cardiovascular fluid–structure interactions with the deforming-spatial-domain/stabilized space–time formulation. *Computer Methods in Applied Mechanics and Engineering* 2006; **195**:1885–1895.
15. Bazilevs Y, Calo VM, Zhang Y, Hughes TJR. Isogeometric fluid–structure interaction analysis with applications to arterial blood flow. *Computational Mechanics* 2006; **38**:310–322.
16. Torii R, Oshima M, Kobayashi T, Takagi K, Tezduyar TE. Influence of wall elasticity in patient-specific hemodynamic simulations. *Computers and Fluids* 2007; **36**:160–168.
17. Tada S, Tarbel JM. Oxygen mass transport in a compliant carotid bifurcation model. *Annals of Biomedical Engineering* 2006; **34**. Available online.
18. Tezduyar TE. Stabilized finite element formulations for incompressible flow computations. *Advances in Applied Mechanics* 1992; **28**:1–44.
19. Tezduyar TE, Behr M, Liou J. A new strategy for finite element computations involving moving boundaries and interfaces—the deforming-spatial-domain/space–time procedure: I. The concept and the preliminary numerical tests. *Computer Methods in Applied Mechanics and Engineering* 1992; **94**:339–351.
20. Tezduyar TE, Behr M, Mittal S, Liou J. A new strategy for finite element computations involving moving boundaries and interfaces—the deforming-spatial-domain/space–time procedure: II. Computation of free-surface flows, two-liquid flows, and flows with drifting cylinders. *Computer Methods in Applied Mechanics and Engineering* 1992; **94**:353–371.

DOI: 10.1002/fld

21. Mittal S, Tezduyar TE. Parallel finite element simulation of 3D incompressible flows—fluid–structure interactions. *International Journal for Numerical Methods in Fluids* 1995; **21**:933–953.
22. Kalro V, Tezduyar TE. A parallel 3D computational method for fluid–structure interactions in parachute systems. *Computer Methods in Applied Mechanics and Engineering* 2000; **190**:321–332.
23. Tezduyar T, Osawa Y. Fluid–structure interactions of a parachute crossing the far wake of an aircraft. *Computer Methods in Applied Mechanics and Engineering* 2001; **191**:717–726.
24. Stein KR, Benney RJ, Tezduyar TE, Leonard JW, Accorsi ML. Fluid–structure interactions of a round parachute: modeling and simulation techniques. *Journal of Aircraft* 2001; **38**:800–808.
25. Tezduyar TE. Computation of moving boundaries and interfaces and stabilization parameters. *International Journal for Numerical Methods in Fluids* 2003; **43**:555–575.
26. Michler C, van Brummelen EH, Hulshoff SJ, de Borst R. The relevance of conservation for stability and accuracy of numerical methods for fluid–structure interaction. *Computer Methods in Applied Mechanics and Engineering* 2003; **192**:4195–4215.
27. van Brummelen EH, de Borst R. On the nonnormality of subiteration for a fluid–structure interaction problem. *SIAM Journal on Scientific Computing* 2005; **27**:599–621.
28. Tezduyar TE, Sathe S, Keedy R, Stein K. Space–time finite element techniques for computation of fluid–structure interactions. *Computer Methods in Applied Mechanics and Engineering* 2006; **195**:2002–2027.
29. Khurram RA, Masud A. A multiscale/stabilized formulation of the incompressible Navier–Stokes equations for moving boundary flows and fluid–structure interaction. *Computational Mechanics* 2006; **38**:403–416.
30. Masud A. Effects of mesh motion on the stability and convergence of ALE based formulations for moving boundary flows. *Computational Mechanics* 2006; **38**:430–439.
31. Kuttler U, Forster C, Wall WA. A solution for the incompressibility dilemma in partitioned fluid–structure interaction with pure Dirichlet fluid domains. *Computational Mechanics* 2006; **38**:417–429.
32. Masud A, Bhanabhagvanwala M, Khurram RA. An adaptive mesh rezoning scheme for moving boundary flows and fluid–structure interaction. *Computers and Fluids* 2007; **36**:77–91.
33. Sawada T, Hisada T. Fluid–structure interaction analysis of the two dimensional flag-in-wind problem by an interface tracking ALE finite element method. *Computers and Fluids* 2007; **36**:136–146.
34. Wall WA, Genkinger S, Ramm E. A strong coupling partitioned approach for fluid–structure interaction with free surfaces. *Computers and Fluids* 2007; **36**:169–183.
35. Tezduyar TE, Sathe S. Modeling of fluid–structure interactions with the space–time finite elements: solution techniques. *International Journal for Numerical Methods in Fluids* 2007. DOI: 10.1002/fld.1430
36. Taylor CL, Yuan Z, Selman WR, Ratcheson RA, Rimm AA. Cerebral arterial aneurysm formation and rupture in 20,767 elderly patients: hypertension and other risk factors. *Journal of Neurosurgery* 1995; **83**:812–819.
37. Karino T, Takeuchi S, Kobayashi N, Motomiya M, Mabuchi S. Fluid dynamics of cerebrovascular disease (in Japanese). *Neurosurgeons* 1993; **12**:15–24.
38. Hughes TJR, Brooks AN. A multi-dimensional upwind scheme with no crosswind diffusion. In *Finite Element Methods for Convection Dominated Flows*, Hughes TJR (ed.), AMD, vol. 34. ASME: New York, 1979; 19–35.
39. Brooks AN, Hughes TJR. Streamline upwind/Petrov–Galerkin formulations for convection dominated flows with particular emphasis on the incompressible Navier–Stokes equations. *Computer Methods in Applied Mechanics and Engineering* 1982; **32**:199–259.
40. Tezduyar TE, Mittal S, Ray SE, Shih R. Incompressible flow computations with stabilized bilinear and linear equal-order-interpolation velocity–pressure elements. *Computer Methods in Applied Mechanics and Engineering* 1992; **95**:221–242.
41. Tezduyar T, Aliabadi S, Behr M, Johnson A, Mittal S. Parallel finite-element computation of 3D flows. *Computer* 1993; **26**:27–36.
42. Tezduyar TE, Aliabadi SK, Behr M, Mittal S. Massively parallel finite element simulation of compressible and incompressible flows. *Computer Methods in Applied Mechanics and Engineering* 1994; **119**:157–177.
43. Tezduyar T, Aliabadi S, Behr M, Johnson A, Kalro V, Litke M. Flow simulation and high performance computing. *Computational Mechanics* 1996; **18**:397–412.
44. Tezduyar TE. CFD methods for three-dimensional computation of complex flow problems. *Journal of Wind Engineering and Industrial Aerodynamics* 1999; **81**:97–116.
45. Tezduyar TE. Finite element methods for flow problems with moving boundaries and interfaces. *Archives of Computational Methods in Engineering* 2001; **8**:83–130.
46. Tezduyar TE. Interface-tracking and interface-capturing techniques for finite element computation of moving boundaries and interfaces. *Computer Methods in Applied Mechanics and Engineering* 2006; **195**:2983–3000.

47. Tezduyar TE. Finite elements in fluids: stabilized formulations and moving boundaries and interfaces. *Computers and Fluids* 2007; **36**:191–206.
48. Tezduyar TE. Finite elements in fluids: special methods and enhanced solution techniques. *Computers and Fluids* 2007; **36**:207–223.
49. Tezduyar TE, Sathe S, Stein K. Solution techniques for the fully-discretized equations in computation of fluid–structure interactions with the space–time formulations. *Computer Methods in Applied Mechanics and Engineering* 2006; **195**:5743–5753.
50. Tezduyar TE. Finite element methods for fluid dynamics with moving boundaries and interfaces. In *Encyclopedia of Computational Mechanics*, *Volume 3*: *Fluids*. Chapter 17, Stein E, De Borst R, Hughes TJR (eds). Wiley: New York, 2004.
51. Tezduyar TE, Behr M, Mittal S, Johnson AA. Computation of unsteady incompressible flows with the finite element methods—space–time formulations, iterative strategies and massively parallel implementations. *New Methods in Transient Analysis*, PVP-vol. 246/AMD-vol. 143. ASME: New York, 1992; 7–24.
52. Loremson WE, Cline HE. Marching cubes: a high resolution 3D surface construction algorithm. *Computer Graphics* 1987; **21**:163–169.
53. Wells Jr RE, Merrill EW. Shear rate dependence of the viscosity of whole blood and plasma. *Science* 1961; **133**:763–764.
54. Womersley JR. Method for the calculation of velocity, rate of flow and viscos drag in arteries when the pressure gradient is known. *Journal of Physiology* 1955; **127**:553–563.

DOI: 10.1002/fld